



## Reactive adsorption and photodegradation of soman and dimethyl methylphosphonate on TiO<sub>2</sub>/nanodiamond composites



Jiří Henych<sup>a,b,\*</sup>, Štěpán Stehlík<sup>c</sup>, Karel Mazanec<sup>d</sup>, Jakub Tolasz<sup>a,b</sup>, Jan Čermák<sup>e</sup>, Bohuslav Rezek<sup>e</sup>, Andreas Mattsson<sup>f</sup>, Lars Österlund<sup>f</sup>

<sup>a</sup> Institute of Inorganic Chemistry of the Czech Academy of Sciences, 250 68 Husinec-Řež, Czech Republic

<sup>b</sup> Faculty of Environment, Králova výšina 7, J.E. Purkyně University in Ústí nad Labem, 400 96 Ústí nad Labem, Czech Republic

<sup>c</sup> Institute of Physics of the Czech Academy of Sciences, Cukrovarnická 10, 162 00 Prague 6, Czech Republic

<sup>d</sup> Military Research Institute, Veslařská 230, 637 00 Brno, Czech Republic

<sup>e</sup> Faculty of Electrical Engineering, Czech Technical University, Technická 2, 166 27 Prague 6, Czech Republic

<sup>f</sup> Department of Engineering Sciences, The Ångström Laboratory, Uppsala University, P.O. Box 534, SE-751 21 Uppsala, Sweden

### ARTICLE INFO

#### Keywords:

Titanium dioxide  
Nanodiamond  
Nanocomposites  
Photocatalysis  
Chemical warfare agents

### ABSTRACT

We report on the synthesis and characterization of TiO<sub>2</sub>/Nanodiamond (ND) nanocomposites for rapid decontamination of chemical warfare agents (CWA) and toxic industrial compounds prepared by a simple water-based, low-temperature method using urea as a homogeneous precipitating agent. The excellent water-compatibility of NDs promoted their good dispersion within the TiO<sub>2</sub> matrix resulting in intergrown TiO<sub>2</sub>/ND nanostructures. NDs with an abundance of oxygen-containing surface moieties increased the porosity of the composites resulting in their three times more efficient spontaneous degradation of the CWA soman in solution compared to pure TiO<sub>2</sub>. In situ DRIFT spectroscopy revealed the enhanced reactive adsorption and solar light photodecomposition of dimethyl methyl phosphonate vapor on TiO<sub>2</sub>/ND. The charge transfer across TiO<sub>2</sub>/ND interfaces that hinder recombination of photo-excited electron-hole pairs was inferred from surface potential measurements. The results indicate that well-dispersed NDs forming heterojunctions together with their high porosity contribute to the reactive properties of the nanocomposites.

### 1. Introduction

Several procedures have been developed for decontamination of toxic organophosphates (OP), including chemical warfare agents (CWA) and toxic industrial compounds (TIC), since they raise serious environmental and security concerns (see Ref. [1] and references therein). This group of chemicals, based on esters of phosphoric acid, include popular insecticides (e.g. parathion or chlorpyrifos) that were widely used and available until the end of the 20<sup>th</sup> century [2]. Interestingly, OP pesticides have a similar chemical structure to the notorious toxic chemical warfare agents (CWA) sarin, soman, tabun, agent VX, and novichok. These agents cause a cholinergic crisis in insects, birds, amphibians and mammals due to inhibition of the acetylcholinesterase enzyme (AChE) by phosphorylation. Inhibition of AChE results in continuous impulse transmission from nerve fibers to smooth and skeletal muscle cells and prevents muscle relaxation, eventually leading to respiratory paralysis [3,4].

Thus, it is essential to prevent human inhalation exposure to the

toxic OPs, especially in the agricultural industry [5], or in the case of a CWA incidence, but also in the indoor air due to the OP-based flame retardant additives [6], or in an aircraft cabin where OPs originate from the turbine and hydraulic oils [7]. For fast and efficient capture and decontamination of the OP from the air, or for removal from natural waters, where they represent a severe environmental threat, deployment of suitable adsorbents is an efficient and inexpensive method [8,9]. Nanomaterials possess exceptional ability to chemically transform adsorbed OP to less toxic or harmless products thanks to their large surface area combined with possible high surface reactivity. The class of nanomaterials that can be activated by light, photocatalytic nanomaterials, and in particular semiconducting oxides, may further be tailored for accelerated degradation. Nanostructured TiO<sub>2</sub> can advantageously utilize both effects while being stable and non-toxic. Other properties, such as particle size and morphology, crystallinity, and surface chemistries, can be further controlled by the preparation methods. Doping of TiO<sub>2</sub> with other elements may lead to further modifications, e.g. enhanced light absorption [10], and decreased

\* Corresponding author at: Institute of Inorganic Chemistry of the Czech Academy of Sciences, 250 68 Husinec-Řež, Czech Republic.  
E-mail address: [henych@iic.cas.cz](mailto:henych@iic.cas.cz) (J. Henych).

recombination rate of electron-hole pairs [11], that both improve the efficiency of photo-induced decomposition (PID).

In recent years, the development of nanocomposites that combine benefits of two or more of the constituent materials in heterojunction [12] has given rise to a new class of nanomaterials with intriguing properties that cannot be achieved by single-component materials or by their simple physical mixing. Depending on the application,  $\text{TiO}_2$  is often combined with other metal oxides, such as  $\text{Cu}_x\text{O}$  [13],  $\text{ZnO}$  [14],  $\text{SnO}_2$  [15],  $\text{Fe}_2\text{O}_3$  [16], metal nanoparticles [17], polymers [18], inorganic carbon low-dimensional materials [19–22], or with recently popular 2D materials such as MXenes [23] to achieve higher photocatalytic and antibacterial activity, or to modify optical, electric, anticorrosion, sensing, structural, or surface properties. In particular, graphene derivatives and carbon nanotubes, each which can be prepared by a range of different methods [24], can substantially improve photocatalytic activity of  $\text{TiO}_2$  [25]. Recent demand for more environmentally friendly synthesis methods have led to the development of new approaches for nanomaterials preparation such as new sonochemical methods [26,27], simple co-precipitation [28], microwave-assisted methods [29], or biosynthesis [30]. As we recently have shown [31],  $\text{TiO}_2/\text{graphene oxide}$  nanocomposites can easily be prepared by simple homogeneous precipitation of  $\text{TiOSO}_4$  water solution with urea at low temperature (up to 100 °C). These nanocomposites were shown to efficiently adsorb and decompose DMMP.

Nanodiamond (ND) is an intriguing carbon nanomaterial that holds great promise in heterogeneous catalysis due to its high surface area, chemical stability, optional doping, and tailorabile surface chemistry [32]. Commercially available so-called “single-digit” detonation nanodiamonds (DND) with a diameter as small as 4–5 nm are produced on an industrial scale by the detonation of explosives, typically a mixture of RDX/TNT 60/40%, in oxygen-deficient conditions [33]. Despite the interesting physical properties of ND materials only a few recent studies report on their use in  $\text{TiO}_2$  nanocomposites. Pastrana-Martínez, et al. prepared  $\text{TiO}_2$  composites with micro- and NDs using a liquid phase deposition method and observed an increased PID of the pharmaceutical water pollutants diphenhydramine and cyanobacterial toxins due to the abundance of oxygen surface species and possible electronic interaction at the ND- $\text{TiO}_2$  interface [34–36]. Atomic layer deposition was employed to prepare ND-supported  $\text{TiO}_2$  thin films that were efficient for total oxidation of toluene under low relative humidity conditions which was ascribed to the hydrophilic nature of the ND surface that facilitates water chemisorption and formation of OH radicals [37].

In this work,  $\text{TiO}_2/\text{ND}$  nanocomposites were prepared by a simple water-based low-temperature (< 100 °C) method from common industrial precursors avoiding the use of expensive solvents or organometallic compounds. The prepared composites were used for the first time for the degradation of highly toxic OP soman and DMMP. The prepared composites substantially enhanced the soman degradation in solution as compared to pure  $\text{TiO}_2$  nanoparticles. Furthermore, in situ diffuse reflectance infrared Fourier transform (DRIFT) spectroscopy showed improved spontaneous dissociation and subsequent photodecomposition of DMMP on  $\text{TiO}_2/\text{ND}$  compared to pure  $\text{TiO}_2$ . The favorable electronic interaction between ND and  $\text{TiO}_2$  resulting in increased surface photovoltage on the  $\text{TiO}_2/\text{ND}$  was revealed by Kelvin probe measurements. Based on the results, a mechanism for the observed ND enhanced spontaneous OP dissociation and subsequent PID is discussed.

## 2. Experimental

### 2.1. Preparation of $\text{TiO}_2/\text{ND}$ composites

ND powder with a nominal size of primary particles of 5 nm was purchased from New Metals and Chemicals (Japan). All other chemicals were supplied by Sigma-Aldrich (Czech Republic) and used as received.

The  $\text{TiO}_2/\text{ND}$  composites were prepared by simple water-based

precipitation method without the use of organometallic compounds, expensive solvents or autoclaving. As we have shown in previous studies, this method is suitable for preparation of nanostructured single [38], or binary oxides [39],  $\text{TiO}_2/\text{graphene oxide}$  composites [31], or cation doping [40,41] of  $\text{TiO}_2$ .

In detail, 1 g of  $\text{TiOSO}_4$  was dissolved in 200 ml distilled warm water (35 °C) acidified with 1 ml of  $\text{H}_2\text{SO}_4$ , and then 10 g of urea was dissolved in the solution. A certain amount of ND powder (according to weight ratio  $\text{TiO}_2/\text{ND}$  - 10:1, 20:1, 40:1, 80:1) was dispersed in 1 l of distilled water by bath sonication (1 h, 300 W), and slowly mixed with  $\text{TiOSO}_4/\text{urea}$  solution. The obtained mixture was heated at 90 °C for 6 h under vigorous stirring. The obtained greyish precipitate was washed with water by decantation several times (until the conductivity of the solution was less than 100 mS/m), filtered, air-dried and annealed at 300 °C for 2 h under ambient air.

### 2.2. Characterization methods

Crystal phase analysis was performed using a Bruker D2 diffractometer equipped with a conventional X-ray tube ( $\text{Cu K}\alpha = 1.5418 \text{ \AA}$  radiation, 30 kV, 10 mA) and the LYNXEYE 1-dimensional detector. The structure, phase composition, and morphology of the powder samples were studied using a FEI Nova NanoSEM 450 and scanning electron microscopes (SEM) with accelerating voltage 5 kV in a high-vacuum mode and high-resolution transmission electron microscopy (HRTEM) was performed with a FEI Talos F200X microscope equipped with energy dispersive X-ray spectroscopy (EDS) elemental mapping. SEM/EDS elemental mapping was acquired using an X-Max<sup>N</sup> EDS detector (Oxford Instruments). For SEM analysis the samples were drop cast from water suspension on the pure silicon wafer and air-dried while holey carbon grid was used for TEM measurements. Raman spectra were recorded using a Renishaw inVia Raman confocal microscope with 532 nm excitation laser and neutral density filters (0.5% transmission). FTIR spectra obtained by averaging 128 scans with spectral resolution  $4 \text{ cm}^{-1}$  were recorded using Nicolet Nexus 670 spectrometer equipped with MCT detector and diffuse reflectance accessory. The specific surface area and morphological properties of the samples were obtained from liquid nitrogen isothermal physisorption measurements using a Micromeritics ASAP 2010 instrument. The samples were evacuated at 150 °C overnight before measurement.

### 2.3. Soman degradation

The decontamination activity of the samples towards soman (GD) was evaluated by the well-established testing procedure [40,42,43]. Briefly, 50 mg of ND/ $\text{TiO}_2$  powder adsorbent dispersed in 400  $\mu\text{L}$  of nonane was placed into a series of glass vials. Into each vial, 150  $\mu\text{L}$  of the substrate solution was added resulting in soman/adsorbent ratio 1/50 mg. The sealed vials were kept in the dark at a constant temperature of 25 °C. At selected times (0, 10, 20, 40, 60, 120, 600, 1200 s) the reaction was terminated by addition of 2-propanol (1.85 mL). The solid adsorbents were separated immediately by centrifugation (5000 rpm, 5 min) and aliquots of the supernatant were analyzed by GC/FPD. Agilent 6890 N gas chromatograph with HP-5 column (5% phenyl methyl siloxane, 30 m × 0.32 mm ID × 0.25  $\mu\text{m}$  film thickness) was used for determination of residual GD concentration. GD used in this study was synthesized in the Military Research Institute, state enterprise in Brno, Czech Republic and its purity was 91,05%.

### 2.4. In situ DRIFTS

Adsorption and photodecomposition of DMMP on the  $\text{TiO}_2/\text{ND}$  composites were investigated by in situ diffuse reflectance infrared spectroscopy (DRIFTS). The experimental setup (schematically depicted in our previous study [44]) comprises a vacuum-pumped FTIR spectrometer (Vertex 80/80v, Bruker, Germany) with a modified reaction

cell (Praying Mantis High Temp. Reaction Chamber, Harrick, USA) connected to a heat controller and gas-supply system as described elsewhere [45]. The IR cell allows combined DRIFTS, gas dosing and photon irradiation of the sample under controlled atmosphere and temperature. Simulated solar light, generated by a high-pressure Xe arc lamp (300 W, Oriel Instruments, USA) with a set of AM1.5 filters and 54 mm long water filter was directed to the cell via a quartz fiber bundle. The output photon power measured by a thermopile detector (Ophir, Israel) was  $169 \text{ mW cm}^{-2}$  in the wavelength region  $200 < \lambda < 800 \text{ nm}$ . Prior to each measurement samples were annealed at  $300^\circ\text{C}$  in a flow of  $100 \text{ ml min}^{-1}$  of synthetic air (Alphagaz, 99.999% purity) for 30 min and cooled to  $25^\circ\text{C}$  in the same gas to remove organic contaminants. Liquid DMMP (97%, GC purity, Sigma-Aldrich) was evaporated at  $62^\circ\text{C}$  and introduced into a gas stream of synthetic air via diffusion tube. Dosing of DMMP was performed for 15 min with subsequent flushing the cell with synthetic air for 15 min before illumination of the sample. Repeated DRIFT spectra with spectral resolution  $4 \text{ cm}^{-1}$  were acquired in 1 min intervals between consecutive measurements (120 co-added spectra). Presented spectra were smoothed by Savitzky-Golay algorithm and baseline corrected applying a polynomial fit to the region of interest.

### 2.5. Kelvin probe

Surface potential measurements were performed by a scanning Kelvin probe (KP Technology) equipped with a golden probe of 2 mm in diameter. The samples were drop-casted on a gold substrate which served as a contact electrode. Solar Lightline A1 solar simulator (Sciencetech, Inc.) calibrated to AM 1.5 spectrum and light intensity was used for sample illumination.

## 3. Results and discussion

### 3.1. Material characterization

Controlled thermal decomposition of urea in  $\text{TiOSO}_4$  water solution leads to precipitation of highly crystalline nanostructured  $\text{TiO}_2$ . Urea is a common homogeneous precipitator, but it also acts as a capping agent that controls the crystallization and size of the particles.  $\text{TiO}_2$ -based nanocomposites with NDs can readily be prepared by the simple addition of ND solution in the reaction mixture containing  $\text{TiOSO}_4$  and urea with subsequent heating of the solution.

Similarly to the graphene oxide, which we used in a recent study [31], the water-compatibility of the NDs employed here allows for the formation of highly stable colloids, making ND a perfect candidate for the water-based urea precipitation method because of the high dispersion of NDs within the sample that can be achieved. The excellent colloidal stability of the used NDs is expressed by their positive zeta potential in acidic to neutral pH range provided by poly-functional surface chemistry including C-H bonds [46]. It is worth mentioning that the ND powder employed in this study is a precursor for manufacturing of well-established commercially available colloid of dispersed primary particles of detonation ND branded as NanoAmando™.

In the XRD pattern of as received ND powder (Fig. 1a), broad diffraction lines observed at  $43.9^\circ$  and  $75.4^\circ$  were assigned to the (111) and (220) planes of diamond phase. The occurrence of a very broad peak at  $\sim 27^\circ$  suggests that the employed ND powder also contains some graphitic phase, either on the ND surfaces or as inclusions in ND aggregates [47]. In the pure  $\text{TiO}_2$  and all  $\text{TiO}_2/\text{ND}$  nanocomposites (Fig. 1a), the anatase phase was identified as the only  $\text{TiO}_2$  polymorph with its characteristic diffraction lines in agreement with the JCPDS card no. 21-1272. The most intense diffraction lines of the diamond phase were found in the composites with  $\text{TiO}_2/\text{ND}$  ratio between 10:1 and 40:1, while at the lowest ND content ( $\text{TiO}_2/\text{ND}$  80:1) only anatase peaks were visible, most likely due to a higher NDs dispersion within the sample. The line-broadening of both the diamond and anatase

phases suggests nanoparticulate morphology of the samples. The mean crystallite size, as estimated from a Rietveld analysis (Table 1), was calculated to be  $10.1 \pm 0.5 \text{ nm}$  for the anatase phase  $\text{TiO}_2$  nanoparticles and  $\sim 5 \text{ nm}$  for the nanodiamonds.

Raman spectroscopy is a powerful method for phase analysis and study of carbon-based nanomaterials. The Raman measurements (Fig. 1b) agree well with the XRD results. The typical anatase Raman modes  $E_g$ ,  $B_{1g}$ ,  $B_{1g} + A_{1g}$ , and  $E_g$  were observed at  $\sim 152$ ,  $397$ ,  $516$ , and  $644 \text{ cm}^{-1}$ , respectively, in all nanocomposites and the pure  $\text{TiO}_2$ . The inset in Fig. 1b shows the ND related Raman  $F_{2g}$  modes. The as-received NDs exhibits an optical phonon line corresponding to symmetric vibrations of the  $\text{sp}^3$  diamond lattice ( $F_{2g}$ ), centered at  $1324 \text{ cm}^{-1}$ , while the broad band ( $1400$ - $1700 \text{ cm}^{-1}$ ) is commonly ascribed to non-diamond  $\text{sp}^2$  carbon phase [48]. Both ND features were also found in the nanocomposites, but the  $F_{2g}$  mode was shifted by  $\sim 5 \text{ cm}^{-1}$  to higher wavenumbers and the graphitic band shifted up by  $\sim 30 \text{ cm}^{-1}$  and became broader. This is most likely due to the air annealing of the composites at  $300^\circ\text{C}$  that caused partial oxidation of NDs and removal of graphitic carbon phase.

Various surface functional groups were found on the surfaces of NDs and  $\text{TiO}_2/\text{ND}$  composites by FTIR spectroscopy (Fig. S1). The bands related to adsorbed water, surface OH groups, carbonyl, carboxyl, various C-H groups, and possibly ether, and ester groups can be assigned according to the literature [49]. The bands are, however, only clearly resolved on bare NDs and composites with the higher ND content ( $\text{TiO}_2/\text{ND}$  10:1), except the vibration band due to scissor mode of adsorbed water at  $1627 \text{ cm}^{-1}$ , which is visible on all samples.

The TEM analysis of the sample  $\text{TiO}_2/\text{ND}$  40:1 (Fig. 1c) shows randomly oriented primary  $\text{TiO}_2$  nanocrystals with size below 10 nm. Strikingly different type of nanoparticles with different shapes and sizes were found on the outer surface of the grains. The lattice spacing found in these particles (0.20 nm) corresponds well with (111) diamond faces, while a 0.35 nm d-spacing was detected in other particles within the same sample and can be identified with the (101) planes of anatase  $\text{TiO}_2$ . The ND particles detected in TEM are larger than the 5 nm grain size estimated from XRD data. This suggests that they consist of aggregated 5 nm primary ND particles. Nevertheless, as evident from TEM, NDs are in close contact with  $\text{TiO}_2$  nanoparticles, thus forming an intergrown structure of  $\text{TiO}_2$  matrix with embedded primary and aggregated NDs. TEM/EDS elemental mapping (Fig. 2) show Ti and O as the main elements in both pure  $\text{TiO}_2$  (Fig. 2a and c) and  $\text{TiO}_2/\text{ND}$  40:1 composite (Fig. 2b and d). Carbon in both samples originate from the grid and ambient atmosphere contamination, nevertheless substantial increase of the carbon amount was observed and the apparent carbon-containing clusters were found in the composites and they were ascribed to ND phase. A similar increase of the carbon amount was observed also by SEM/EDS analysis (Fig. S2 in Supplementary data).

The relatively small primary nanoparticle size corresponds well with the high specific surface area (SSA) of the samples determined from nitrogen physisorption isotherm BET analysis (Table 1). Slightly higher SSA  $291 \text{ m}^2 \text{ g}^{-1}$  was obtained for ND powder compared with pure titania ( $255 \text{ m}^2 \text{ g}^{-1}$ ). With the addition of small amounts of NDs the SSA slightly decreases, but there is a trend of increasing SSA with increasing ND content, approximately reaching the SSA of the pure  $\text{TiO}_2$  ( $255 \text{ m}^2 \text{ g}^{-1}$ ) at a 10:1  $\text{TiO}_2/\text{ND}$  mixing ratio. On the other hand, the total pore volume ( $V_{\text{pore}}$ ) of the ND powder ( $1.24 \text{ m}^3 \text{ g}^{-1}$ ) was almost seven times larger than for pure  $\text{TiO}_2$  ( $0.24 \text{ m}^3 \text{ g}^{-1}$ ) and it is related to a significantly larger mean pore diameter of NDs (22.3 nm) compared with titania (3.7 nm). Importantly, ND addition increased  $V_{\text{pore}}$  of the composites by 16, 29, 38, and 63% for the composites with  $\text{TiO}_2/\text{ND}$  ratio 80, 40, 20, and 10:1, respectively. The adsorption isotherms and pore size distribution of the samples are shown in Fig. 3a and b. As-received ND powder is characterized by a Type IV isotherm associated with mesoporous materials. Although the observed H3 hysteresis loop is often related to slit-shaped pores of layered materials, it can also point to a low degree of pore curvature and non-rigidity of the

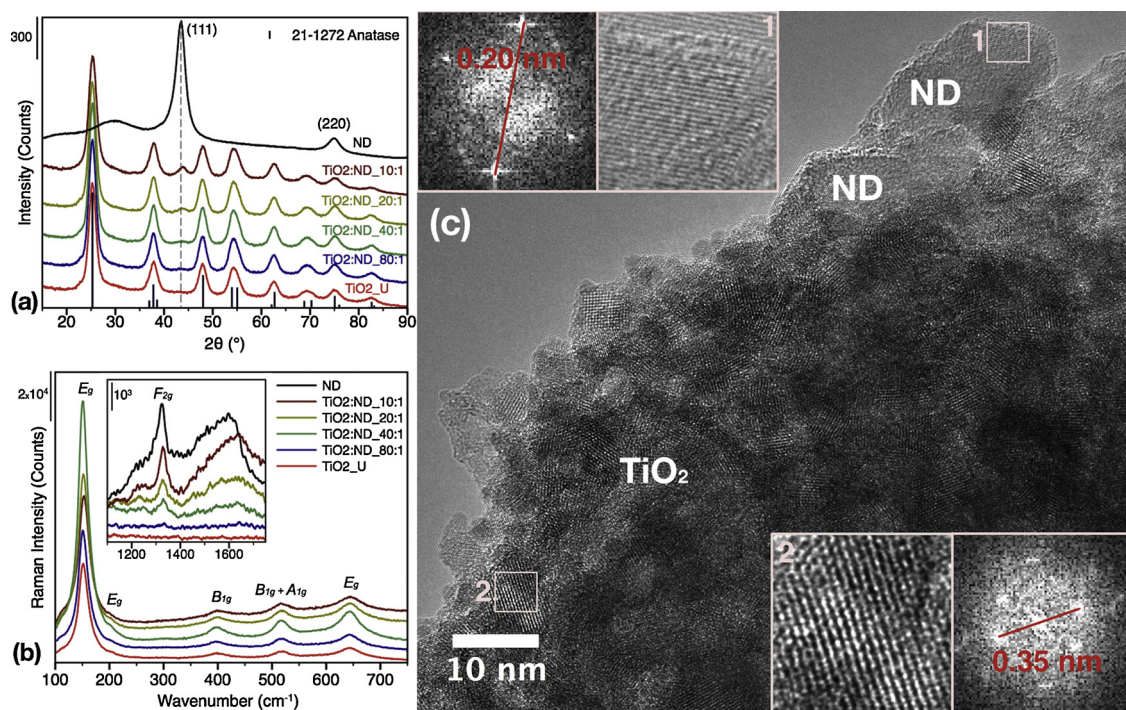


**Fig. 1.** a) XRD diffractograms, b) Raman spectra, and c) TEM image with corresponding FFT and HRTEM images shown as insets of pure TiO<sub>2</sub>, ND and TiO<sub>2</sub>/ND nanocomposites.

**Table 1**

Specific surface area (SSA), total pore volume ( $V_{\text{pore}}$ ) of the prepared samples obtained from nitrogen physisorption using BET and BJH analysis. Average crystallite size of anatase calculated from XRD data using Rietveld refinement.

Sample	SSA, $\text{m}^2/\text{g}$	$V_{\text{pore}}$ , $\text{cm}^3/\text{g}$	Mean pore diameter, nm	Anatase average crystallite size (XRD), nm
TiO <sub>2</sub> _U	255	0.24	3.7	10.1
TiO <sub>2</sub> :ND_80:1	232	0.28	4.8	10.4
TiO <sub>2</sub> :ND_40:1	236	0.31	5.3	10.3
TiO <sub>2</sub> :ND_20:1	240	0.33	5.5	10.6
TiO <sub>2</sub> :ND_10:1	252	0.39	6.1	10.2
ND	291	1.62	22.3	–

aggregate structure [50] that corresponds well with the nature of ND powder, which is formed by loosely aggregated primary nanoparticles. Pure titania and all TiO<sub>2</sub>:ND nanocomposites maintained Type IV isotherm exhibiting an H2 hysteresis loop typical for mesoporous materials with interparticle pores forming heterogeneous pore networks and ill-defined pores. As can be seen from the pore size distribution in Fig. 3b, mesopores with sizes between 2–10 nm dominate in all samples with a considerable contribution of micropores below 1 nm.

SEM micrographs (Fig. 4 and Fig. S3) show that pure TiO<sub>2</sub> primary nanoparticles (Fig. 4a) form spherical aggregates that are a few hundred nm in size. As received NDs (Fig. 4f) form irregular agglomerates of primary ND particles. The addition of NDs induces distinctive morphological changes in all TiO<sub>2</sub>:ND nanocomposites (Fig. 4b–e). At lower ND concentration, (TiO<sub>2</sub>:ND 80:1 and 40:1 in Fig. 4b and c) spherical aggregates are retained and smaller particles and agglomerates of NDs are dispersed on their surfaces. In contrast, higher ND amounts (TiO<sub>2</sub>:ND 20:1 and 10:1 in Fig. 4d and e) promote the formation of smaller and irregular agglomerates of TiO<sub>2</sub> with NDs, which is also reflected in the higher SSA.

### 3.2. Degradation of soman

The nanocomposites were evaluated for decontamination of the CWA soman (GD) in solution (Fig. 5). Soman degradation was evaluated by the empirical Eq. 1 for the adsorptive degradation of CWAs as described previously assuming a fast and slow first-order degradation process: [42,43]

$$q_t = q_1 e^{(-k_1 t)} + q_2 e^{(-k_2 t)} + q_0, \quad (1)$$

where  $q_t$  is the remaining quantity of toxic agent at time  $t$ ,  $q_1$  and  $q_2$  represent model parameters expressing the ratio of the faster and slower process involved,  $k_1$  and  $k_2$  are pseudo-first order rate constants representing a fast and slow reaction, respectively, and  $q_0$  is the residual fraction of the unconverted CWA. The parameters of the model are listed in Table 2. The initial rate of conversion (IRC) was determined from the first derivative of the degradation curve at  $t = 0$  as the slope of the tangent line.

The results are consistent with previous studies [38,40], which show that pure titania prepared by urea precipitation exhibits excellent decontamination capability for GD. The GD conversion degree (CD) exceeded 82% after 60 s and the residual GD concentration further decreased to 8% after 120 s. Contrary, pure ND powder possesses negligible conversion activity (CD = 7.7% at 60 s). Interestingly, the composites with low to moderate ND concentration (TiO<sub>2</sub>:ND 80:1, 40:1, 20:1) showed the highest decontamination activity as evident from their rate constants, IRC, and CD shown in Table 2. Sample TiO<sub>2</sub>:ND 40:1 exhibited the highest decontamination efficiency with approximately three times larger rate constants, IRC and CD exceeding 99% within 60 s. Even the smallest amount of ND addition (TiO<sub>2</sub>:ND 80:1) considerably improved the decontamination efficiency of the composite and its kinetic parameters are comparable to the sample with moderate ND concentration (TiO<sub>2</sub>:ND 20:1). At higher ND concentration (TiO<sub>2</sub>:ND 10:1) the efficiency decreased significantly.

The low decontamination activity of pure NDs and the composites with the highest amount of NDs (TiO<sub>2</sub>:ND 10:1) suggests that titania is the main active component for GD decontamination. This is consistent with the proposed degradation mechanism where the reactive

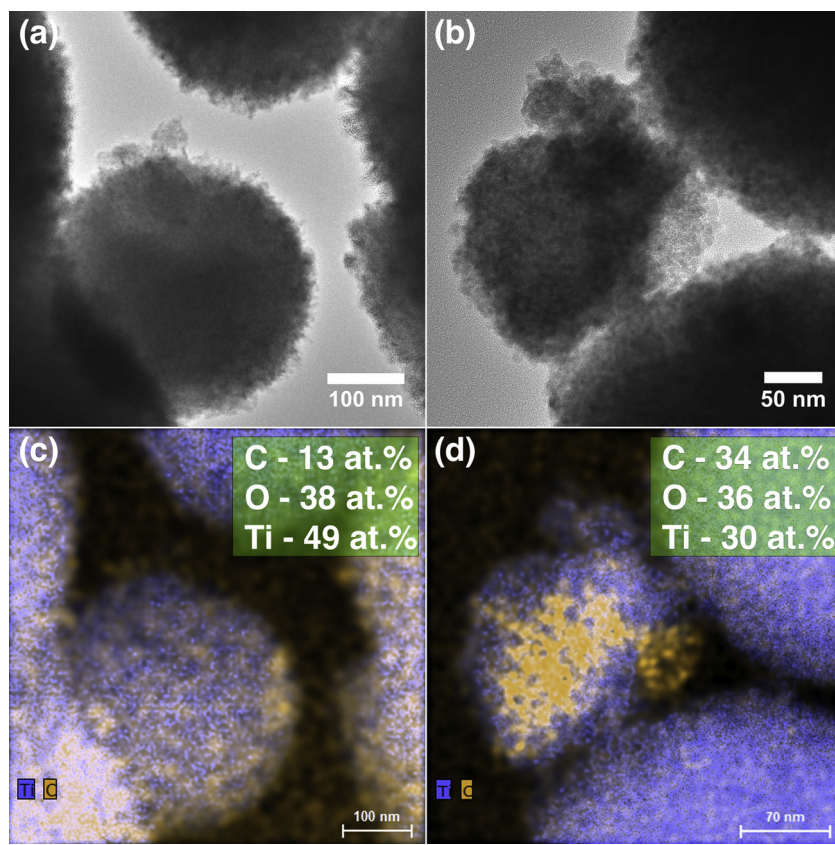


**Fig. 2.** TEM with EDS elemental mapping of a,c) pure  $\text{TiO}_2$  and b,d)  $\text{TiO}_2$ :ND 40:1 nanocomposites.

adsorption of GD involves unsaturated metal cationic sites (acting as Lewis acid) interacting with electron-rich phosphoryl oxygen (acting as Lewis base) of GD and then surface  $-\text{OH}$  groups attack of the P central atom in organophosphate molecule by  $\text{S}_{\text{N}}2$  nucleophilic substitution mechanism [42]. To explain the high decontamination activity of the samples with low amounts of NDs ( $\text{TiO}_2$ :ND 20:1, 40:1, 80:1), we note that addition of NDs increases the mean pore diameter and the total pore volume of the composites that improves the availability of the surface for GD adsorption.

However, the observation that the sample with the highest ND amount exhibits low decontamination activity despite much higher total pore volume and larger pores compared with pure NDs, suggests that other effects are also involved. ND particles contain graphitic phase on their surfaces (as evident from XRD and Raman data) and various hydrophilic surface chemical groups (mainly hydroxyl and single- and double-bonded carbon-oxygen groups) [51] that may contribute to the dissociation of GD molecule.

Thus, we ascribe the main improvement of GD degradation to the synergistic interaction between  $\text{TiO}_2$ , that provides unsaturated cationic sites for the initial adsorption of GD, and NDs that promote GD degradation due to the presence of various hydrophilic surface chemical groups (e.g.  $-\text{OH}$ ) together with overall larger total pore volume. Importantly, a proper  $\text{TiO}_2$ :ND ratio ensures that a sufficiently large  $\text{TiO}_2$  surface is available for the adsorption and surface chemical reactions while also providing synergistic effects of hydrophilic groups on NDs. At higher ND concentration, ND particles block the Ti cationic sites and consequently hinder GD adsorption.

A comparison of the soman degradation efficiency of the prepared  $\text{TiO}_2$ /ND composites with some other nanostructured materials from the recent works using the same experimental procedure is presented in Table 3.

### 3.3. Adsorption of DMMP

**Fig. 6** shows DRIFT spectra as a function of time during DMMP gas dosing into the IR reaction cell. The spectra of pure NDs and sample with high ND content ( $\text{TiO}_2$ :ND 10:1) show very low signal-to-noise ratio due to the very low adsorption capacity for DMMP (not shown), which was also seen when these samples were exposed to soman as shown in the previous section. DMMP adsorption surface products were assigned according to our previous studies [31,41,54]. In the  $\nu(\text{OH})$  stretching region of pure  $\text{TiO}_2$  (**Fig. 6a**), the negative bands centered at  $3733 \text{ cm}^{-1}$  due to terminal OH groups, and  $3674 \text{ cm}^{-1}$  due to bridging OH groups are formed as DMMP interacts with isolated Ti–OH surface groups and depletes them [55,56].

In the spectra of the composites, the  $\nu(\text{OH})$  bands become sharper and the low frequency band shifts up from  $3674 \text{ cm}^{-1}$  to  $3684 \text{ cm}^{-1}$ , while the  $3733 \text{ cm}^{-1}$  remains at the same frequency. Moreover, two additional negative bands (at  $3654$  and  $3633 \text{ cm}^{-1}$ ) develop on the  $\text{TiO}_2$ /ND samples. These results further indicate that the ND particles are well dispersed on  $\text{TiO}_2$  and supply specific ND–OH surface groups that contribute to reactive adsorption of DMMP.

In the  $\nu(\text{C}-\text{H})$  stretching region, besides the asymmetrical and symmetrical vibrations of methyl (at  $3003$  and  $2925 \text{ cm}^{-1}$ ) and methoxy groups (at  $2960$  and  $2860 \text{ cm}^{-1}$ ) belonging to non-dissociated DMMP, an additional band assigned to Ti surface coordinated methoxy groups ( $2828 \text{ cm}^{-1}$ ) was clearly visible in all samples. This, together with related bands in the fingerprint region, indicates that DMMP dissociates and methoxy groups are cleaved from DMMP molecule and adsorb on the other available surface sites. It is evident that this band is distinctively more intense on all  $\text{TiO}_2$ /ND composites confirming their higher reactivity for DMMP degradation. Comparisons of the integrated  $\nu(\text{C}-\text{H})$  band intensity normalized to the SSA for each sample (**Table 4**) confirm an enhanced adsorption of DMMP on all  $\text{TiO}_2$ /ND composites. Furthermore, the ratio of Ti-coordinated methoxy groups (i.e.

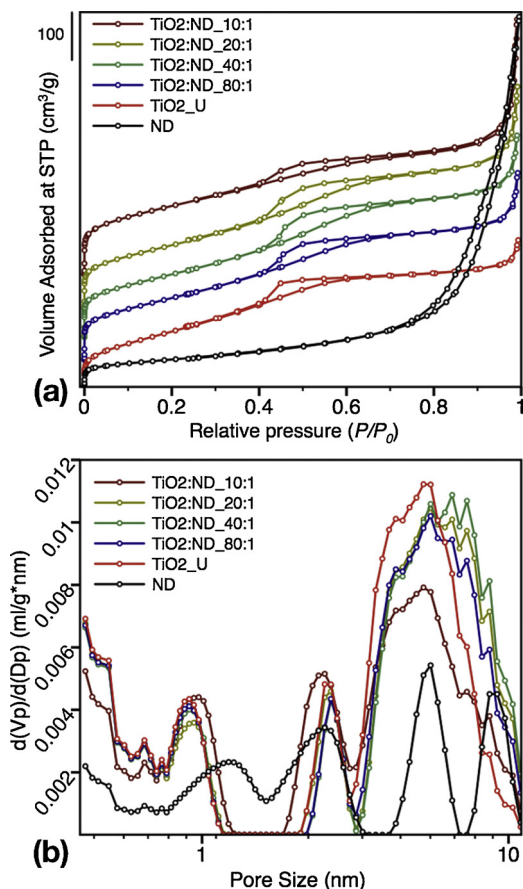


Fig. 3. a) N<sub>2</sub> adsorption/desorption isotherms, and b) pore-size distribution obtained from BJH analysis.

dissociated DMMP) and methoxy groups of non-dissociated DMMP was three times larger on all nanocomposites clearly demonstrating that NDs promoted spontaneous dissociation of adsorbed DMMP on TiO<sub>2</sub>/

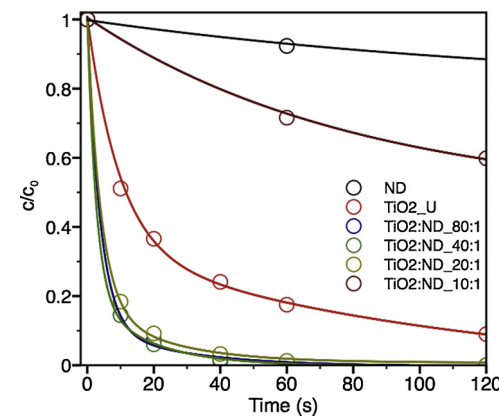


Fig. 5. Degradation of soman on TiO<sub>2</sub>, ND and TiO<sub>2</sub>/ND composites. The solid lines are least-square best fits of the data to Eq. 1.

ND composites.

In the fingerprint region (Fig. 6b), typical bands for adsorbed DMMP and its dissociation products can be seen. The shoulder of the broad band at 1665 cm<sup>-1</sup> that is related to coordinatively bonded HCOOH to Lewis acid sites and bands at 1594 and 1560 cm<sup>-1</sup> due to  $\nu_a(\text{COO}-)$  modes of differently coordinated formates are distinctively more intense on TiO<sub>2</sub>/ND composites, again showing their higher reactivity towards DMMP dissociation compared to pure TiO<sub>2</sub>.

Interestingly, the bands due to  $\nu(\text{P=O})$  stretching modes, often the most intense bands in the spectra of adsorbed DMMP (as in the case of TiO<sub>2</sub>/graphene oxide composites in our recent study [31]) are almost missing in the spectra of TiO<sub>2</sub>/ND samples. Contrary, the bands related to methyl group attached to the central P atom in the DMMP molecule became much stronger on the composites. This can be explained by high reactivity of the composites since the surface coordinated P=O species can be converted to a variety of single-bonded P-O<sub>x</sub> species that would be seen in the 900 to 1100 cm<sup>-1</sup> region.

However, they are not seen in the spectra as the IR absorption in TiO<sub>2</sub> results in low signal-to-noise ratio in this region. Furthermore, the high intensities of the 1175 cm<sup>-1</sup> band that is usually ascribed to the

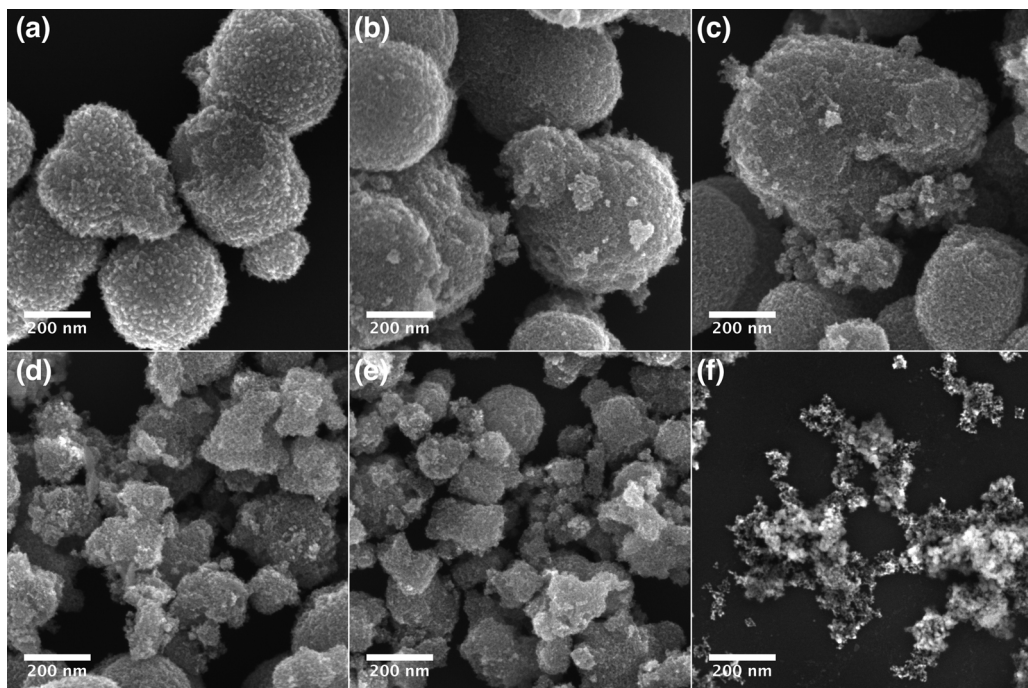


Fig. 4. SEM analysis of a) TiO<sub>2</sub>, b) TiO<sub>2</sub>:ND 80:1, c) TiO<sub>2</sub>:ND 40:1, d) TiO<sub>2</sub>:ND 20:1, e) TiO<sub>2</sub>:ND 10:1, f) as-received NDs.

**Table 2**

Kinetic model parameters for soman degradation.

Sample	Degradation of Soman					
	$k_1$ (s <sup>-1</sup> ) <sup>a</sup>	$k_2$ (s <sup>-1</sup> ) <sup>a</sup>	Initial rate of conversion $\times 10^{-4}$ (mol L <sup>-1</sup> s <sup>-1</sup> ) <sup>b</sup>	Residue ( $q_0$ ) at time 120 s	Conversion degree at time 60 s (%)	Quality $R^2$
TiO <sub>2</sub> _U	0.127 (0.03)	0.013 (0.04)	1.9	0.08	82.5	0.9904
TiO <sub>2</sub> :ND 80:1	0.264 (0.046)	0.039 (0.054)	5.6	< 0.01	99.5	0.9944
TiO <sub>2</sub> :ND 40:1	0.375 (0.053)	0.057 (0.032)	6.8	< 0.01	99.4	0.9976
TiO <sub>2</sub> :ND 20:1	0.253 (0.031)	0.045 (0.028)	5.0	< 0.01	98.7	0.9981
TiO <sub>2</sub> :ND 10:1	0.086 (0.098)	0.003 (0.002)	0.2	0.60	28.4	0.9810
ND	0.054 (0.016)	0.001 (0.001)	< 0.1	0.88	7.7	0.9302

<sup>a</sup> Standard errors given in parentheses.<sup>b</sup> Calculated as the slope of the tangent line of the experimental curves at t = 0.

$\nu(\text{CH}_3\text{-P})$  modes can be related to DMMP dissociation, since it is realized through cleavage of methoxy groups that can cause “free” movement of the methyl group on the central P atom and thus higher intensity of the related bands in the spectra. In contrast, in pure TiO<sub>2</sub> all DMMP bands including the  $\nu(\text{P=O})$  stretch have relatively low intensity suggesting lower adsorption capacity.

### 3.4. Photo-induced degradation of DMMP

Fig. 7 shows time-resolved DRIFT spectra acquired on nanocomposites with pre-adsorbed DMMP during simulated solar light illumination. The rapid decrease of DMMP related bands and a formation of the new, qualitatively similar intermediate species were observed on the pure TiO<sub>2</sub> (Fig. 7a, b) and TiO<sub>2</sub>:ND 80:1 (Fig. 7c, d) during illumination. Similarly, almost identical spectra as those from the TiO<sub>2</sub>:ND 80:1 sample were obtained for samples with moderate ND content (Fig. S4 a-d). In the OH region (Fig. 7a and c), production of water in the course of photo-degradation causes (i) progressive decrease of the negative bands related to isolated Ti-OH groups as they are consumed by self-association of OH groups, and (ii) increase of the broad band between 3600–3400 cm<sup>-1</sup> belonging to O-H stretch in water and hydrogen-bonded OH groups.

Photo-induced degradation of the DMMP (and its thermal dissociation products) on TiO<sub>2</sub> results in further oxidation of the methyl and methoxy groups and produce both surface adsorbed formic acid, formate ions, carbonates, and water, as well as gaseous products such as methanol, CO<sub>2</sub> and water vapor [41,57]. OPs are known to adsorb on metal oxides via the phosphoryl oxygen at either Lewis acid cation sites or Brönstedt acid hydroxyl groups bonded to cation sites [58,59]. On TiO<sub>2</sub> it has been reported that electrophilic attack on the P atom by hydroxyls leads to dissociation of the P=O bond and defragmentation of methyl groups yielding surface methoxy and subsequently surface formate [54,58]. These decomposition products are also identified in this work in the in situ DRIFTS measurements in Fig. 7. A plausible mechanism for the efficient degradation of OP would, therefore, be hydroxyl promoted OP dissociation, where the production of active OH species is stimulated by UV light.

The adsorption structure of intermediate species is strongly dependent on the adsorbate structure and bonding to TiO<sub>2</sub> as well as experimental conditions (e.g. temperature and humidity) [44,60]. The apparent broadening and shift of the decreasing  $\nu_s(\text{CH}_3\text{O})$  band at

2870 cm<sup>-1</sup> (more distinct on the composite samples) is caused by interference with the band related to the formate intermediate species that are formed in the initial stage of PID and subsequently are also decomposed after prolonged illumination [44].

Unlike TiO<sub>2</sub>-based graphene oxide composites [44], NDs do not significantly change the mechanism of PID as evident from the comparison of the spectra of pure TiO<sub>2</sub> (Fig. 7b) and TiO<sub>2</sub>/ND composites (Fig. 7d) in the fingerprint region (1800–1100 cm<sup>-1</sup>). The spectra are dominated by the intense bands with apparent maxima at 1611 and 1582 cm<sup>-1</sup>. The first band is formed by the superposition of the water  $\delta(\text{H}-\text{O}-\text{H})$  mode produced during PID and  $\nu_a(\text{O}-\text{C}-\text{O})$  vibrational modes of formate species and surface coordinated formic acid [41].

The latter band was assigned to  $\nu_a(\text{O}-\text{C}-\text{O})$  vibrations due to coordinated HCOO<sup>-</sup> ions associated with the corresponding  $\delta(\text{CH})$  and  $\nu_s(\text{O}-\text{C}-\text{O})$  modes at 1382 and 1361 cm<sup>-1</sup>, respectively [61]. Two intense bands are gradually formed during the course of PID at ~1288 and 1251 cm<sup>-1</sup> suggesting they are related to the most stable or final products of PID. The band at 1288 cm<sup>-1</sup> is ambiguous but it was previously assigned to  $\nu(\text{P=O})$  stretching related to the hydrogen-bonded phosphoric acid moiety that is retained on the surface after PID [57]. The vibrational mode at 1251 cm<sup>-1</sup> is most likely due to the C-O stretch in a carbonate or carboxylate decomposition product [44]. Note that the relative intensities of these two bands are distinctively higher on the TiO<sub>2</sub>/ND composites compared to pure TiO<sub>2</sub>.

### 3.5. Kinetics of DMMP photodecomposition

The overall degradation efficiency of the PID can be estimated from pseudo-first order reaction kinetics by plotting  $\ln(A/A_0)$  as a function of illumination time (Fig. 8), where A is the integrated absorbance area of the  $\nu(\text{C-H})$  bands region from DRIFTS (~3050–2800 cm<sup>-1</sup>) at time t. The initial decomposition rate is seen to obey first-order reaction kinetics during the first 5 min:

$$-\frac{d\theta_{\text{DMMP}}}{dt} = k_{\text{dec}} \theta_{\text{DMMP}} \quad (2)$$

where  $\theta_{\text{DMMP}}$  is the surface coverage of adsorbed DMMP (including surface coordinated Ti methoxy groups) and is proportional to A, and  $k_{\text{dec}}$  is the rate constant for the overall decomposition of adsorbed C-H containing species determined from a linear least-squares fit to the experimental data in Fig. 8.

**Table 3**Comparison of the degradation efficiency against soman of the prepared TiO<sub>2</sub>/ND composites and other selected nanostructured materials.

Sample	$k_1$ (s <sup>-1</sup> )	$k_2$ (s <sup>-1</sup> )	Degree of conversion after 60 s (%)	Reference
TiO <sub>2</sub> :ND_40:1	0.375	0.057	99.4	This work
MnO <sub>2</sub>	0.037	0.001	< 50	Štengl et al. [43]
Ferrate(VI)/(III) composite	0.007	—	~40	Zboril et al. [52]
Zr doped TiO <sub>2</sub>	0.065	0.009	> 99	Štengl et al. [53]
Ge doped TiO <sub>2</sub>	0.745	0.010	99.5	Štengl et al. [40]
CeO <sub>2</sub>	0.658	0.007	> 90	Janoš et al. [42]

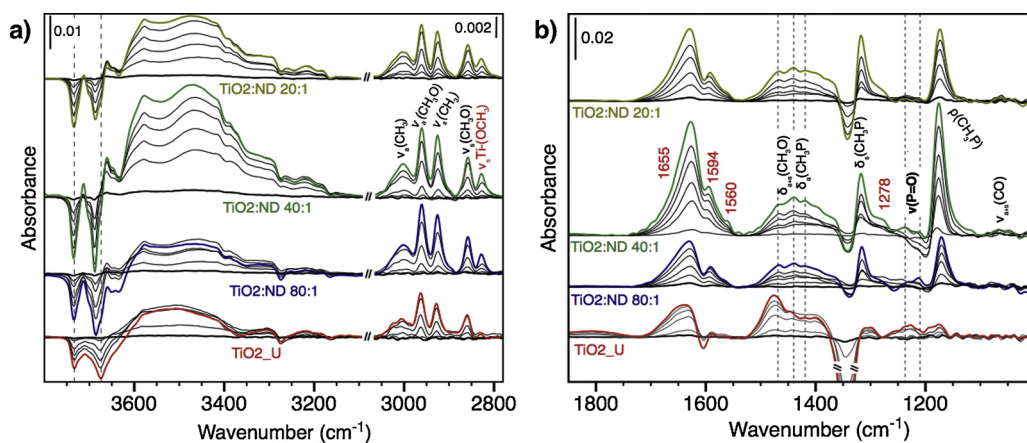


**Fig. 6.** Time-resolved DRIFTS spectra of DMMP adsorption on  $\text{TiO}_2/\text{ND}$  nanocomposites; a) OH and C–H bands region, b) fingerprint region. Thick color lines represent the adsorption spectra after 15 min of DMMP dosing and 15 min flushing of the reaction cell with synthetic air.

**Table 4**

Specific surface area (SSA) normalized absorbance on  $\text{TiO}_2$  and  $\text{TiO}_2/\text{ND}$  composites. Columns from left: Integrated absorbance of all  $\nu(\text{C}-\text{H})$  bands due to DMMP; the methoxy  $\nu_s(\text{CH}_3\text{O})$  band due to DMMP; the  $\nu_s(\text{Ti}-\text{OCH}_3)$  band due to methoxy groups cleaved from DMMP; and the ratio of SSA normalized integrated area of Ti-coordinated methoxy to DMMP methoxy groups before the start of illumination.

Sample	SSA normalized $\nu(\text{CH}_3)$ area	SSA normalized integrated area of $\nu_s(\text{CH}_3\text{O})$ groups	SSA normalized integrated area of $\nu_s(\text{Ti}-\text{OCH}_3)$ groups	Integrated area ratio $\nu_s(\text{Ti}-\text{OCH}_3)/\nu_s(\text{CH}_3\text{O})$
$\text{TiO}_2\text{-U}$	0.6411	0.1257	0.0188	0.15
$\text{TiO}_2\text{-ND}_{80:1}$	1.4529	0.2642	0.1173	0.44
$\text{TiO}_2\text{-ND}_{40:1}$	1.6805	0.3057	0.1567	0.51
$\text{TiO}_2\text{-ND}_{20:1}$	1.2078	0.2657	0.1440	0.54

In the later stage of PID ( $t > 10$  min), the PID kinetics is changed, which is expected since strongly bonded intermediates accumulate and block the active sites (and is also observed for soman degradation, see Eq. 1). The reactive adsorption and subsequent photodecomposition thus can lead to the partial deactivation of the catalyst and strategies for its surface recovery should be investigated and applied. High temperature and/or chemical or sonochemical treatment with suitable solvents may be applicable, but care must be taken to avoid irreversible deactivation of the nanocomposite surface. As evident from the SSA normalized rate constants (Table 5), the initial degradation rate was 1.6 to 1.8 times higher on all  $\text{TiO}_2/\text{ND}$  composites compared to pure  $\text{TiO}_2$ . The results are consistent with the GD degradation where the samples with the low ND content ( $\text{TiO}_2/\text{ND}$  80–20:1) also show the best degradation efficiency.

Apparently, NDs in the composites induce several effects that lead to more efficient (photo)degradation of DMMP. We have shown that NDs improve the adsorption capacity of the composites and thereby a larger amount of the adsorbed DMMP can be decomposed by photo-induced reactive species. Furthermore, NDs, similarly to graphene and other carbon materials, can act as an electron shuttle of electrons from  $\text{TiO}_2$  thus avoiding electron-hole recombination and thereby contributing to a better overall PID efficiency [62]. Moreover, as we show above, NDs also significantly enhance spontaneous dissociation of DMMP, probably by introducing more oxygen-rich surface groups that promote cleavage of methoxy groups from DMMP molecules. This leads to the formation of a higher amount of  $\text{Ti}-\text{OCH}_3$  surface methoxy groups.

As evident from the time-resolved DRIFT spectra (Fig. 7a and c, and Fig. S4a and S4b) and plots of the individual  $\nu(\text{C}-\text{H})$  bands as a function of time (Fig. 9), the individual functional groups follow different reaction kinetics. Similar data were obtained for all samples and thus only

a representative plot for  $\text{TiO}_2/\text{ND}$  80:1 is shown in Fig. 9. Note that due to the interference of the bands (especially for  $\nu_s(\text{CH}_3\text{O})$ ) and low signal-to-noise ratio, only the well-resolved bands  $\nu_a(\text{CH}_3\text{O})$ ,  $\nu_a(\text{CH}_3)$ , and  $\nu_s(\text{Ti}-\text{OCH}_3)$  were included in the plot. It is evident that the  $\text{Ti}-\text{OCH}_3$  surface groups are the most susceptible species for photo-oxidation, followed by methyl and remaining methoxy groups in good agreement with our previous studies of  $\text{TiO}_2/\text{GO}$  composites [44]. Thus, the higher overall PID efficiency on the ND/ $\text{TiO}_2$  nanocomposites is attributed to substantially more  $\text{Ti}-\text{OCH}_3$  surface groups (that are more prone to photooxidation) due to spontaneous dissociation of DMMP.

### 3.6. Kelvin probe measurements

Kelvin probe in combination with illumination by the solar simulator (AM 1.5) was employed to study surface photovoltage (SPV) on neat  $\text{TiO}_2$  and  $\text{TiO}_2/\text{ND}$  composites (Fig. 10a). Time-resolved photovoltage measurements show the formation of the SPV on  $\text{TiO}_2$  as electron-hole pairs are formed upon its illumination. Interestingly, a substantial increase of photovoltage was observed with increasing ND content in the composites that can be explained by two mechanisms: (i) reduced charge recombination and/or trapping by spatial charge separation of the excited electron-hole pairs at the  $\text{TiO}_2/\text{ND}$  interface (Route I in Fig. 10b), and (ii) photosensitization, i.e. more efficient generation of free charge by additional light absorption and generation charge carriers in the  $\text{TiO}_2/\text{ND}$  composites (Route II in Fig. 10b). The energy levels were obtained from the Kelvin probe work function measurements and the literature data [63,64]. The band diagrams are drawn according to established guidelines [65]. NDs can also absorb some of the incident light via optical excitation of defects and surface states, and thereby can provide additional holes to  $\text{TiO}_2$  due to the suitable band alignment and band bending (Route II in Fig. 10b). The Fermi levels are equilibrated within the composite due to direct contact between  $\text{TiO}_2$  and ND. The vacuum level of  $\text{TiO}_2$  is about 0.1 eV lower due to the work function difference thus supporting that an electron depletion region is formed in  $\text{TiO}_2$  next to the NDs that can act as electron acceptors. Therefore, NDs may help spatially separate electron-hole pairs that are generated upon  $\text{TiO}_2$  bandgap illumination. Both mechanisms (i) and (ii) lead to negative charging of NDs in the composites, which is measured as the increasing negative photovoltage by the Kelvin probe.

It is however observed that at high ND concentration ( $\text{TiO}_2/\text{ND}$  10:1) SPV decreases as ND coverage becomes too thick suggesting that for the observed synergistic effect close physical contact between  $\text{TiO}_2$  and highly dispersed NDs is essential. It is also noted that SPV increases up to 20:1  $\text{TiO}_2/\text{ND}$  ratio while the photocatalytic activity is highest at

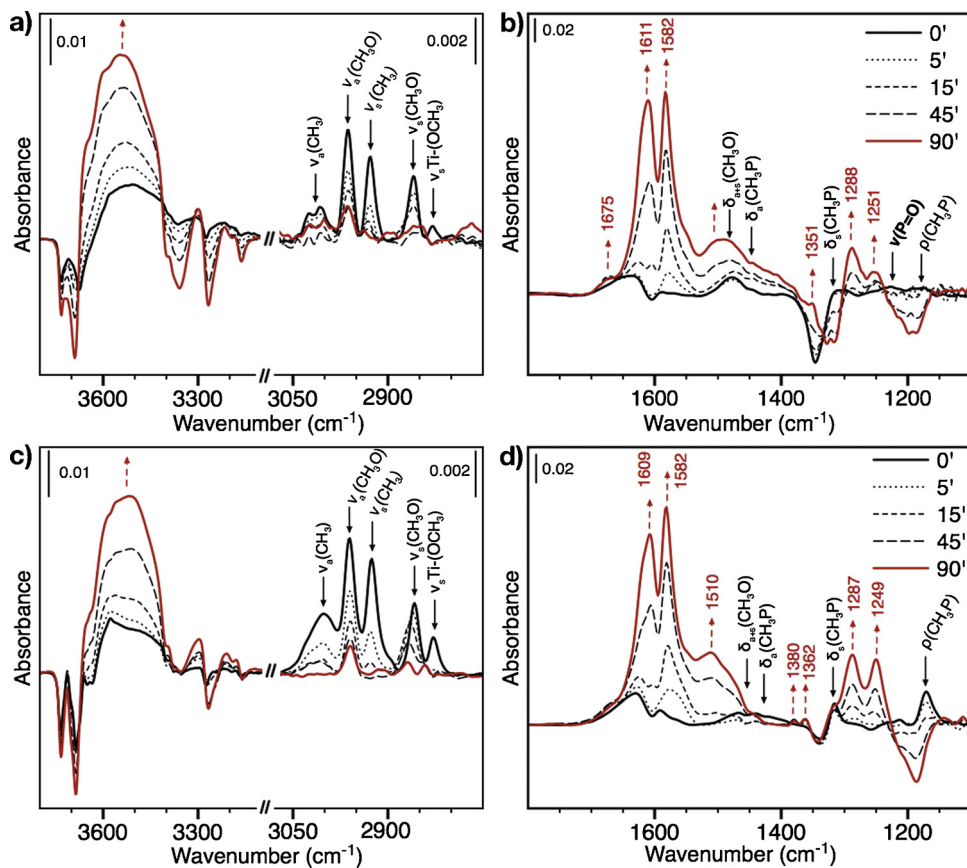


Fig. 7. Selected time-resolved DRIFTS spectra of photo-induced decomposition of DMMP on a-b) TiO<sub>2</sub>, c-d) TiO<sub>2</sub>:ND 80:1 sample.

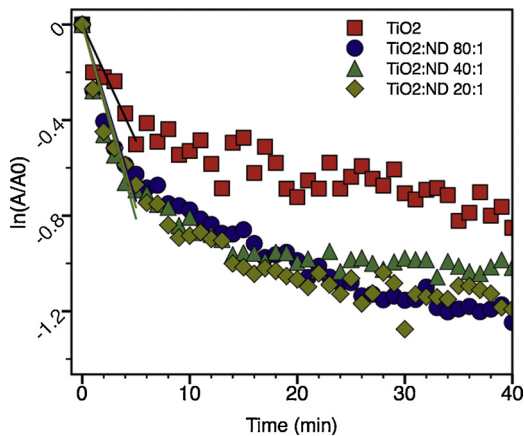


Fig. 8. Normalized logarithmic decay of the  $\nu(\text{C}-\text{H})$  stretching region as a function of illumination time representing overall photodegradation efficiency of TiO<sub>2</sub> and TiO<sub>2</sub>/ND nanocomposites.

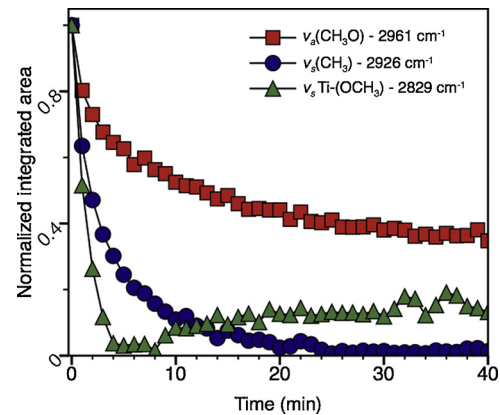


Fig. 9. Decrease of the selected individual C-H bands as a function of illumination time representing different decomposition kinetics of adsorbed species on TiO<sub>2</sub>:ND 80:1 sample.

40:1 ratio. It implies that improving the photo-generation and reducing carrier recombination is not the only important effect to achieve the enhanced photocatalytic activity. Instead, we conjecture that it is a balance between electronic TiO<sub>2</sub>/ND interfacial effects, available TiO<sub>2</sub> surface sites, suitable texture and porosity that determines the efficiency of the TiO<sub>2</sub>/ND composites. We remark that up-scaling may for these reasons be non-trivial and require several iterations and modifications to optimize the final nanocomposite. In particular, careful control of the experimental conditions such as starting concentration and ratio of the precursors, efficient dispersion of the ND powder in the reaction mixture, controlled slow co-precipitation and stirring rate must be properly secured.

Table 5

First order rate constants ( $k_{dec}$ ) and SSA normalized rate constants ( $k_{SSA}$ ) for photo-induced degradation of DMMP determined from the integrated  $\nu(\text{C}-\text{H})$  bands describing the overall initial decomposition rate of adsorbed species on TiO<sub>2</sub> and TiO<sub>2</sub>/ND composites.

Sample	$k_{dec}$ , min <sup>-1</sup>	$k_{SSA} \times 10^2$ , min <sup>-1</sup> m <sup>-2</sup>
TiO <sub>2</sub> _U	0.0973	0.0382
TiO <sub>2</sub> :ND_80:1	0.1477	0.0637
TiO <sub>2</sub> :ND_40:1	0.1625	0.0689
TiO <sub>2</sub> :ND_20:1	0.1531	0.0608

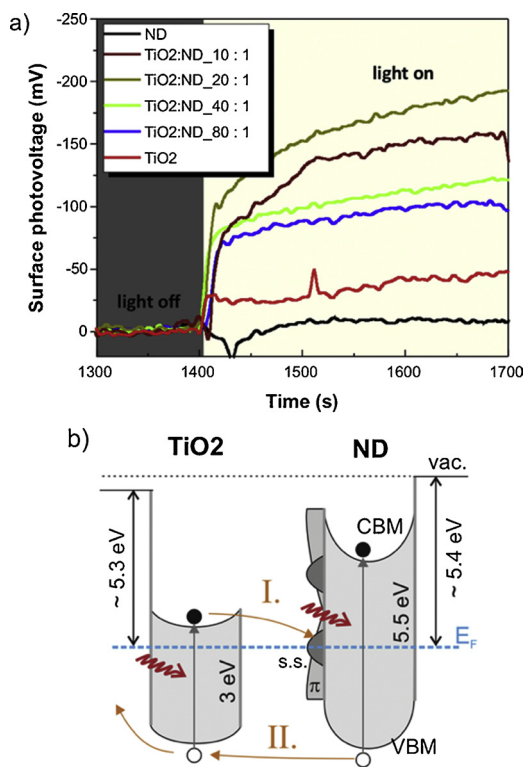


**Fig. 10.** a) Time-resolved photovoltage measurements on NDs, TiO<sub>2</sub>, and TiO<sub>2</sub>-ND nanocomposites by Kelvin probe. b) Simplified scheme of band energy levels and charge transfer process in the TiO<sub>2</sub>-ND composites under illumination. Route I – NDs help dissociate photo-excited electrons-holes in TiO<sub>2</sub>. Route II – NDs provide additional holes to TiO<sub>2</sub> (via defects or surface states related light absorption).

#### 4. Conclusions

The TiO<sub>2</sub>/ND nanocomposites were successfully prepared by a simple water-based homogeneous precipitation reaction with urea. As expected, the excellent water-compatibility of NDs was advantageous for good dispersion of ND within the TiO<sub>2</sub> to form homogeneous intergrown nanostructure of TiO<sub>2</sub> matrix with embedded primary and aggregated NDs. The prepared composites with low to moderate ND content showed substantially improved surface degradation efficacy against the CWA soman in a solution. In situ DRIFTS study of DMMP gas adsorption revealed improved adsorption capacity of the composites compared to pure TiO<sub>2</sub>. Interestingly, ND addition did not lead to a substantial increase of the TiO<sub>2</sub>/ND composites surface area but significantly modified texture and increased pore volume of the composites that resulted in increased adsorption capacity. Importantly, the results confirmed the unique electronic properties of ND as showed the substantially increased formation of surface photovoltage on TiO<sub>2</sub>/ND composites compared to pure TiO<sub>2</sub> measured by Kelvin Probe. Thus, similarly to other carbon nanomaterials, NDs in the TiO<sub>2</sub>/ND composites were shown to considerably improved the degradation efficiency by several effects, i) improved adsorption of DMMP, ii) initial spontaneous dissociation of DMMP to products that are more prone to photooxidation, and iii) beneficial electronic interfacial TiO<sub>2</sub>-ND properties that results in charge separation of photo-excited electron-hole pairs associated with an increased surface photovoltage. The presented results introduce nanodiamonds (ND) as water-compatible, stable, non-toxic and readily available material that can easily be applied in synergy with TiO<sub>2</sub> to achieve efficient (photo)degradation of toxic compounds.

#### Declaration of Competing Interest

The authors declare that they have no known competing financial interests or personal relationships that could have appeared to influence the work reported in this paper.

#### Acknowledgements

This study was supported by the Czech Academy of Sciences through project no. MSM200321601. The work is supported by Operational Programme Research, Development and Education financed by European Structural and Investment Funds and the Czech Ministry of Education, Youth and Sports (Projects No. SOLID21 - CZ.02.1.01/0.0/0.0/16\_019/0000760 and CAP - CZ.02.1.01/0.0/0/15\_003/0000464). S.S. acknowledges the Czech Science Foundation (GAČR) grant number 18-11711Y. L.Ö. and A.M. acknowledge Swedish research council grant number 2016-05904. Authors would like to thank to Jan Demel for N<sub>2</sub> physisorption measurements. The SEM/EDS elemental mapping was carried out at UCEEB CTU.

#### Appendix A. Supplementary data

Supplementary material related to this article can be found, in the online version, at doi:<https://doi.org/10.1016/j.apcatb.2019.118097>.

#### References

- [1] Y.J. Jang, K. Kim, O.G. Tsay, D.A. Atwood, D.G. Churchill, Update 1 of: destruction and detection of chemical warfare agents, Chem. Rev. 115 (2015) PR1-PR76, <https://doi.org/10.1021/acs.chemrev.5b00402>.
- [2] J.R. Roberts, J.R. Reigart, Recognition and management of pesticide poisonings, Recognit. Manag. Pestic. Poisonings, sixth, U.S. Environmental Protection Agency, Washington, DC, 2013 p. 272.
- [3] A. Frioulet, F. Rieger, D. Goudou, G. Amitai, P. Taylor, Interaction of an organophosphate with a peripheral site on acetylcholinesterase, Biochemistry 29 (1990) 914–920, <https://doi.org/10.1021/bi00456a010>.
- [4] J. Bajgar, Organophosphates/nerve agent poisoning: Mechanism of action, diagnosis, prophylaxis, and treatment, Adv. Clin. Chem. 38 (2004) 151–216, [https://doi.org/10.1016/s0065-2423\(04\)38006-6](https://doi.org/10.1016/s0065-2423(04)38006-6).
- [5] M.G. Robson, S. Jaipream, P. Visuthismajarn, W. Siriwong, M. Borjan, Inhalation exposure of organophosphate pesticides by vegetable growers in the bang-rieng subdistrict in Thailand, J. Environ. Public Health 2009 (2009), <https://doi.org/10.1155/2009/452373>.
- [6] F. Yang, J. Ding, W. Huang, W. Xie, W. Liu, Particle size-specific distributions and preliminary exposure assessments of organophosphate flame retardants in office air particulate matter, Environ. Sci. Technol. 48 (2014) 63–70, <https://doi.org/10.1021/es403186z>.
- [7] K. Solbu, H.L. Daee, R. Olsen, S. Thorud, D.G. Ellingsen, T. Lindgren, B. Bakke, E. Lundanes, P. Molander, Organophosphates in aircraft cabin and cockpit air - Method development and measurements of contaminants, J. Environ. Monit. 13 (2011) 1393–1403, <https://doi.org/10.1039/c0em00763c>.
- [8] J.G. Ekerdt, K.J. Klabunde, J.R. Shapley, J.M. White, J.T. Yates, Surface chemistry of organophosphorus compounds, J. Phys. Chem. 92 (1988) 6182–6188, <https://doi.org/10.1021/j100333a005>.
- [9] E. Galarraga, R. Gehr, Phosphorus removal from wastewaters: experimental and theoretical support for alternative mechanisms, Water Res. 31 (1997) 328–338, [https://doi.org/10.1016/S0043-1354\(96\)00256-4](https://doi.org/10.1016/S0043-1354(96)00256-4).
- [10] V. Etacheri, C. Di Valentini, J. Schneider, D. Bahnenmann, S.C. Pillai, Visible-light activation of TiO<sub>2</sub> photocatalysts: advances in theory and experiments, J. Photochem. Photobiol. C Photochem. Rev. (2015) 1–29, <https://doi.org/10.1016/j.jphotochemrev.2015.08.003>.
- [11] L.G. Devi, R. Kavitha, A review on non metal ion doped titania for the photocatalytic degradation of organic pollutants under UV/solar light: role of photo-generated charge carrier dynamics in enhancing the activity, Appl. Catal. B Environ. 140–141 (2013) 559–587, <https://doi.org/10.1016/j.apcatb.2013.04.035>.
- [12] J. Low, J. Yu, M. Jaroniec, S. Wageh, A.A. Al-Ghamdi, Heterojunction photocatalysts, Adv. Mater. 29 (2017) 1601694, , <https://doi.org/10.1002/adma.201601694>.
- [13] X. Qiu, M. Miyachi, K. Sunada, M. Minoshima, M. Liu, Y. Lu, D. Li, Y. Shimodaira, Y. Hosogi, Y. Kuroda, K. Hashimoto, Hybrid Cu xO/TiO<sub>2</sub> nanocomposites as risk-reduction materials in indoor environments, ACS Nano 6 (2012) 1609–1618, <https://doi.org/10.1021/nn2045888>.
- [14] C. Cheng, A. Amini, C. Zhu, Z. Xu, H. Song, N. Wang, Enhanced photocatalytic performance of TiO<sub>2</sub>-ZnO hybrid nanostructures, Sci. Rep. 4 (2014), <https://doi.org/10.1038/srep04181>.
- [15] X. Xu, G. Yang, J. Liang, S. Ding, C. Tang, H. Yang, W. Yan, G. Yang, D. Yu, Fabrication of one-dimensional heterostructured TiO<sub>2</sub>@SnO<sub>2</sub> with enhanced photocatalytic activity, J. Mater. Chem. A 2 (2014) 116–122, <https://doi.org/10.1039/c3ta12863f>.
- [16] J. Liu, J. Meeprasert, S. Namuangruk, K. Zha, H. Li, L. Huang, P. Maitarad, L. Shi,

- D. Zhang, Facet-activity relationship of TiO<sub>2</sub> in Fe<sub>2</sub>O<sub>3</sub>/TiO<sub>2</sub> nanocatalysts for selective catalytic reduction of NO with NH<sub>3</sub>: in situ DRIFTS and DFT studies, *J. Phys. Chem. C* 121 (2017) 4970–4979, <https://doi.org/10.1021/acs.jpcc.6b11175>.
- [17] Y. Yu, W. Wen, X.Y. Qian, J. Bin Liu, J.M. Wu, UV and visible light photocatalytic activity of Au/TiO<sub>2</sub> 2 nanofores with Anatase/Rutile phase junctions and controlled Au locations, *Sci. Rep.* 7 (2017), <https://doi.org/10.1038/srep41253>.
- [18] H. Shi, Y. He, Y. Pan, H. Di, G. Zeng, L. Zhang, C. Zhang, A modified mussel-inspired method to fabricate TiO<sub>2</sub> decorated superhydrophilic PVDF membrane for oil/water separation, *J. Membr. Sci.* 506 (2016) 60–70, <https://doi.org/10.1016/j.memsci.2016.01.053>.
- [19] H. Yu, Y. Zhao, C. Zhou, L. Shang, Y. Peng, Y. Cao, L.Z. Wu, C.H. Tung, T. Zhang, Carbon quantum dots/TiO<sub>2</sub> composites for efficient photocatalytic hydrogen evolution, *J. Mater. Chem. A* 2 (2014) 3344–3351, <https://doi.org/10.1039/c3ta14108j>.
- [20] S.J. Gao, Z. Shi, W. Bin Zhang, F. Zhang, J. Jin, Photoinduced superwetting single-walled carbon nanotube/TiO<sub>2</sub> ultrathin network films for ultrafast separation of oil-in-water emulsions, *ACS Nano* 8 (2014) 6344–6352, <https://doi.org/10.1021/nn501851a>.
- [21] L. Jiang, Z. Ren, S. Chen, Q. Zhang, X. Lu, H. Zhang, G. Wan, Bio-derived three-dimensional hierarchical carbon-graphene-TiO<sub>2</sub> as electrode for supercapacitors, *Sci. Rep.* 8 (2018), <https://doi.org/10.1038/s41598-018-22742-7>.
- [22] N.R. Khalid, A. Majid, M.B. Tahir, N.A. Niaz, S. Khalid, Carbonaceous-TiO<sub>2</sub> nano-materials for photocatalytic degradation of pollutants: a review, *Ceram. Int.* 43 (2017) 14552–14571, <https://doi.org/10.1016/j.ceramint.2017.08.143>.
- [23] J. Low, L. Zhang, T. Tong, B. Shen, J. Yu, TiO<sub>2</sub>/MXene Ti3C2 composite with excellent photocatalytic CO<sub>2</sub> reduction activity, *J. Catal.* 361 (2018) 255–266, <https://doi.org/10.1016/j.jcat.2018.03.009>.
- [24] W.W. Liu, S.P. Chai, A.R. Mohamed, U. Hashim, Synthesis and characterization of graphene and carbon nanotubes: a review on the past and recent developments, *J. Ind. Eng. Chem.* 20 (2014) 1171–1185, <https://doi.org/10.1016/j.jiec.2013.08.028>.
- [25] B. Tang, H. Chen, H. Peng, Z. Wang, W. Huang, Graphene modified TiO<sub>2</sub> composite photocatalysts: mechanism, progress and perspective, *Nanomaterials* 8 (2018) 105, <https://doi.org/10.3390/nano8020105>.
- [26] T. Gholami, M. Salavati-Niasari, M. Bazarganipour, E. Noori, Synthesis and characterization of spherical silica nanoparticles by modified Stöber process assisted by organic ligand, *Superlattices Microstruct.* 61 (2013) 33–41, <https://doi.org/10.1016/j.spmi.2013.06.004>.
- [27] M. Esmaili-Zare, M. Salavati-Niasari, A. Sobhani, Simple sonochemical synthesis and characterization of HgSe nanoparticles, *Ultrason. Sonochem.* 19 (2012) 1079–1086, <https://doi.org/10.1016/j.ultsonch.2012.01.013>.
- [28] S. Zinatloo-Ajabshir, M. Salavati-Niasari, Nanocrystalline Pr6O11: synthesis, characterization, optical and photocatalytic properties, *New J. Chem.* 39 (2015) 3948–3955, <https://doi.org/10.1039/c4nj02106a>.
- [29] N. Mir, M. Salavati-Niasari, F. Davar, Preparation of ZnO nanoflowers and Zn glycerolate nanoplates using inorganic precursors via a convenient route and application in dye sensitized solar cells, *Chem. Eng. J.* 181–182 (2012) 779–789, <https://doi.org/10.1016/j.cej.2011.11.085>.
- [30] M. Goudarzi, N. Mir, M. Mousavi-Kamazani, S. Bagheri, M. Salavati-Niasari, Biosynthesis and characterization of silver nanoparticles prepared from two novel natural precursors by facile thermal decomposition methods, *Sci. Rep.* (2016), <https://doi.org/10.1038/srep32539>.
- [31] J. Henych, V. Štengl, A. Mattsson, J. Tolasz, L. Österlund, Chemical warfare agent simulant DMMP reactive adsorption on TiO<sub>2</sub>/graphene oxide composites prepared via titanium peroxo-complex or urea precipitation, *J. Hazard. Mater.* 359 (2018) 482–490, <https://doi.org/10.1016/j.jhazmat.2018.07.095>.
- [32] V.N. Mochalin, O. Shenderova, D. Ho, Y. Gogotsi, The properties and applications of nanodiamonds, *Nat. Nanotechnol.* 7 (2012) 11–23, <https://doi.org/10.1038/nnano.2011.209>.
- [33] V.Y. Dolmatov, Detonation-synthesis nanodiamonds: synthesis, structure, properties and applications, *Russ. Chem. Rev.* 76 (2007) 339–360, <https://doi.org/10.1070/rcc2007v07n04abeh003643>.
- [34] L.M. Pastrana-Martínez, S. Morales-Torres, S.A.C. Carabineiro, J.G. Buijnsters, J.L. Faria, J.L. Figueiredo, A.M.T. Silva, Nanodiamond-TiO<sub>2</sub> composites for heterogeneous photocatalysis, *ChemPlusChem* 78 (2013) 801–807, <https://doi.org/10.1002/cplu.201300094>.
- [35] M.J. Sampayo, L.M. Pastrana-Martínez, A.M.T. Silva, J.G. Buijnsters, C. Han, C.G. Silva, S.A.C. Carabineiro, D.D. Dionysiou, J.L. Faria, Nanodiamond TiO<sub>2</sub> composites for photocatalytic degradation of microcystin-LA in aqueous solutions under simulated solar light, *RSC Adv.* 5 (2015) 58363–58370, <https://doi.org/10.1039/c5ra08812g>.
- [36] L.M. Pastrana-Martínez, S. Morales-Torres, S.A.C. Carabineiro, J.G. Buijnsters, J.L. Figueiredo, A.M.T. Silva, J.L. Faria, Photocatalytic activity of functionalized nanodiamond-TiO<sub>2</sub> composites towards water pollutants degradation under UV/Vis irradiation, *Appl. Surf. Sci.* 458 (2018) 839–848, <https://doi.org/10.1016/j.apsusc.2018.07.102>.
- [37] K.D. Kim, N.K. Dey, H.O. Seo, Y.D. Kim, D.C. Lim, M. Lee, Photocatalytic decomposition of toluene by nanodiamond-supported TiO<sub>2</sub> prepared using atomic layer deposition, *Appl. Catal. A Gen.* 408 (2011) 148–155, <https://doi.org/10.1016/j.apcata.2011.09.019>.
- [38] V. Štengl, J. Henych, P. Janos, M. Skoumal, Nanostructured metal oxides for stoichiometric degradation of chemical warfare agents, *Rev. Environ. Contam. Toxicol.* 236 (2016) 239–258.
- [39] J. Henych, V. Štengl, M. Slušná, T. Matys Grygar, P. Janoš, P. Kuráň, M. Šťastný, Degradation of organophosphorus pesticide parathion methyl on nanostructured titania-iron mixed oxides, *Appl. Surf. Sci.* 344 (2015) 9–16, <https://doi.org/10.1016/j.apsusc.2015.02.181>.
- [40] V. Štengl, T.M. Grygar, F. Opluštík, T. Němec, Ge4 + doped TiO<sub>2</sub> for stoichiometric degradation of warfare agents, *J. Hazard. Mater.* 227–228 (2012) 62–67, <https://doi.org/10.1016/j.jhazmat.2012.05.007>.
- [41] A. Mattsson, C. Leijon, V. Štengl, S. Bakardjieva, F. Opluštík, P.O. Andersson, L. Österlund, Photodegradation of DMMP and CEES on zirconium doped titania nanoparticles, *Appl. Catal. B-Environ.* 92 (2009) 401–410, <https://doi.org/10.1016/j.apcatb.2009.08.020>.
- [42] P. Janoš, J. Henych, O. Pelant, V. Pilařová, L. Vrtoch, M. Kormunda, K. Mazanec, V. Štengl, Cerium oxide for the destruction of chemical warfare agents: a comparison of synthetic routes, *J. Hazard. Mater.* 304 (2016), <https://doi.org/10.1016/j.jhazmat.2015.10.069>.
- [43] V. Štengl, D. Králová, F. Opluštík, T. Němec, Mesoporous manganese oxide for warfare agents degradation, *Microporous Mesoporous Mater.* 156 (2012) 224–232, <https://doi.org/10.1016/j.micromeso.2012.02.031>.
- [44] J. Henych, A. Mattsson, J. Tolasz, V. Štengl, L. Österlund, Solar light decomposition of warfare agent simulant DMMP on TiO<sub>2</sub>/graphene oxide nanocomposites, *Catal. Sci. Technol.* 9 (2019) 1816–1824, <https://doi.org/10.1039/c9cy00059c>.
- [45] T. van der Meulen, A. Mattsson, L. Österlund, A comparative study of the photocatalytic oxidation of propane on anatase, rutile, and mixed-phase anatase-rutile TiO<sub>2</sub> nanoparticles: role of surface intermediates, *J. Catal.* 251 (2007) 131–144, <https://doi.org/10.1016/j.jcat.2007.07.002>.
- [46] T. Petit, L. Puskar, T. Dolenko, S. Choudhury, E. Ritter, S. Burikov, K. Laptinskii, Q. Brzustowski, U. Schade, H. Yuzawa, M. Nagasaka, N. Kosugi, M. Kurzyp, A. Venoyes, H. Girard, J.C. Arnal, E. Osawa, N. Nunn, O. Shenderova, E.F. Aziz, Unusual water hydrogen bond network around hydrogenated nanodiamonds, *J. Phys. Chem. C* 121 (2017) 5185–5194, <https://doi.org/10.1021/acs.jpcc.b700271>.
- [47] G.S. Yur'ev, V.Y. Dolmatov, X-ray diffraction study of detonation nanodiamonds, *J. Superhard Mater.* 32 (2010) 311–328, <https://doi.org/10.3103/s1063457610050035>.
- [48] V.I. Korepanov, Ho. Hamaguchi, E. Osawa, V. Ermolenkov, I.K. Lednev, B.J.M. Etzold, O. Levinson, B. Zousman, C.P. Epperla, H.C. Chang, Carbon structure in nanodiamonds elucidated from Raman spectroscopy, *Carbon N. Y.* 121 (2017) 322–329, <https://doi.org/10.1016/j.carbon.2017.06.012>.
- [49] T. Petit, L. Puskar, FTIR spectroscopy of nanodiamonds: methods and interpretation, *Diam. Relat. Mater.* 89 (2018) 52–66, <https://doi.org/10.1016/j.diamond.2018.08.005>.
- [50] K.S.W. Sing, R.T. Williams, Physisorption hysteresis loops and the characterization of nanoporous materials, *Adsorp. Sci. Technol.* 22 (2004) 773–782, <https://doi.org/10.1260/0263617053499032>.
- [51] X. Xu, Z. Yu, Y. Zhu, B. Wang, Influence of surface modification adopting thermal treatments on dispersion of detonation nanodiamond, *J. Solid State Chem.* 178 (2005) 688–693, <https://doi.org/10.1016/j.jssc.2004.12.025>.
- [52] R. Zboril, M. Andrlík, F. Opluštík, L. Machala, J. Tucek, J. Filip, Z. Marusák, V.K. Sharma, Treatment of chemical warfare agents by zero-valent iron nanoparticles and ferrate(VI)/(III) composite, *J. Hazard. Mater.* 211–212 (2012) 126–130, <https://doi.org/10.1016/j.jhazmat.2011.10.094>.
- [53] V. Štengl, S. Bakardjieva, N. Murafa, F. Opluštík, L. Österlund, A. Mattsson, P.O. Andersson, Warfare agents degradation on zirconium doped titania, *Microsc. Microanal.* 15 (2009) 1038–1039, <https://doi.org/10.1017/S1431927609097360>.
- [54] A. Kiselev, A. Mattsson, M. Andersson, A.E.C. Palmqvist, L. Österlund, Adsorption and photocatalytic degradation of diisopropyl fluorophosphate and dimethyl methylphosphonate over dry and wet rutile TiO<sub>2</sub>, *J. Photochem. Photobiol. A-Chem.* 184 (2006) 125–134, <https://doi.org/10.1016/j.jphotochem.2006.04.005>.
- [55] H. Lin, J. Long, Q. Gu, W. Zhang, R. Ruan, Z. Li, X. Wang, In situ IR study of surface hydroxyl species of dehydrated TiO<sub>2</sub>: towards understanding pivotal surface processes of TiO<sub>2</sub> photocatalytic oxidation of toluene, *Phys. Chem. Chem. Phys.* 14 (2012) 9468–9474, <https://doi.org/10.1039/c2cp40893g>.
- [56] A. Davydov, The nature of oxide surface centers, in: Chichester (Ed.), *Mol. Spectrosc. Oxide Catal. Surfaces*, John Wiley & Sons, Ltd, 2003, pp. 27–179, <https://doi.org/10.1002/0470867981.ch2>.
- [57] C.N. Rusu, J.T. Yates, Photooxidation of dimethyl methylphosphonate on TiO<sub>2</sub> powder, *J. Phys. Chem. B* 104 (2000) 12299–12305, <https://doi.org/10.1021/jp002562a>.
- [58] C.N. Rusu, J.T. Yates, Adsorption and decomposition of dimethyl methylphosphonate on TiO<sub>2</sub>, *J. Phys. Chem. B* 104 (2000) 12292–12298, <https://doi.org/10.1021/jp002560q>.
- [59] P. Mäkie, P. Persson, L. österlund, Adsorption of trimethyl phosphate and triethyl phosphate on dry and water pre-covered hematite, maghemite, and goethite nanoparticles, *J. Colloid Interface Sci.* 392 (2013) 349–358, <https://doi.org/10.1016/j.jcis.2012.10.012>.
- [60] L. Österlund, Fourier-transform infrared and Raman spectroscopy of pure and doped TiO<sub>2</sub> photocatalysts, *Sol. Hydrol. Nanotechnol.* John Wiley & Sons, Ltd, 2010, pp. 189–238, <https://doi.org/10.1002/9780470823996.ch8>.
- [61] F.P. Rotzinger, J.M. Kesselman-Truttmann, S.J. Hug, V. Shklover, M. Grätzel, Structure and vibrational Spectrum of formate and acetate adsorbed from aqueous solution onto the TiO<sub>2</sub> rutile (110) surface, *J. Phys. Chem. B* 108 (2004) 5004–5017, <https://doi.org/10.1021/jp0360974>.
- [62] Q. Huang, S. Tian, D. Zeng, X. Wang, W. Song, Y. Li, W. Xiao, C. Xie, Enhanced photocatalytic activity of chemically bonded TiO<sub>2</sub>/graphene composites based on the effective interfacial charge transfer through the C-Ti bond, *ACS Catal.* 3 (2013) 1477–1485, <https://doi.org/10.1021/cs400080w>.
- [63] J. Schneider, M. Matsuoaka, M. Takeuchi, J. Zhang, Y. Horiochi, M. Anpo, D.W. Bahnemann, Understanding TiO<sub>2</sub> photocatalysis: mechanisms and materials, *Chem. Rev.* 114 (2014) 9919–9986, <https://doi.org/10.1021/cr5001892>.
- [64] B. Rezek, C.E. Nebel, Kelvin force microscopy on diamond surfaces and devices, *Diam. Relat. Mater.* (2005) 466–469, <https://doi.org/10.1016/j.diamond.2005.01.041>.
- [65] J. Čermák, Y. Koide, D. Takeuchi, B. Rezek, Spectrally dependent photovoltages in Schottky photodiode based on (100) B-doped diamond, *J. Appl. Phys.* 115 (2014), <https://doi.org/10.1063/1.4864420>.

Update

**Applied Catalysis B: Environmental**

Volume 261, Issue , February 2020, Page

DOI: <https://doi.org/10.1016/j.apcatb.2019.118263>



Contents lists available at ScienceDirect

## Applied Catalysis B: Environmental

journal homepage: [www.elsevier.com/locate/apcatb](http://www.elsevier.com/locate/apcatb)



### Corrigendum

## Corrigendum to “Reactive adsorption and photodegradation of soman and dimethyl methylphosphonate on TiO<sub>2</sub>/nanodiamond composites” [Appl. Catal. B: Environ. 259 (2019) 118097]

Jiří Henych<sup>a,b,\*</sup>, Štěpán Stehlík<sup>c</sup>, Karel Mazanec<sup>d</sup>, Jakub Tolasz<sup>a,b</sup>, Jan Čermák<sup>c</sup>, Bohuslav Rezek<sup>e</sup>, Andreas Mattsson<sup>f</sup>, Lars Österlund<sup>f</sup>



<sup>a</sup> Institute of Inorganic Chemistry of the Czech Academy of Sciences, 250 68 Husinec-Řež, Czech Republic

<sup>b</sup> Faculty of Environment, Králova výšina 7, J.E. Purkyně University in Ústí nad Labem, 400 96, Ústí nad Labem, Czech Republic

<sup>c</sup> Institute of Physics of the Czech Academy of Sciences, Cukrovarnická 10, 162 00, Prague 6, Czech Republic

<sup>d</sup> Military Research Institute, Veslařská 230, 637 00, Brno, Czech Republic

<sup>e</sup> Faculty of Electrical Engineering, Czech Technical University, Technická 2, 166 27 Prague 6, Czech Republic

<sup>f</sup> Department of Engineering Sciences, The Ångström Laboratory, Uppsala University, P.O. Box 534, SE-751 21, Uppsala, Sweden

The authors regret erroneously stated affiliation of Jan Čermák as

<sup>e</sup>Faculty of Electrical Engineering, Czech Technical University, Technická 2, 166 27 Prague 6, Czech Republic.

Correct affiliation of Jan Čermák is: <sup>c</sup>Institute of Physics of the

Czech Academy of Sciences, Cukrovarnická 10, 162 00 Prague 6, Czech Republic.

The authors would like to apologise for any inconvenience caused.

DOI of original article: <https://doi.org/10.1016/j.apcatb.2019.118097>

\* Corresponding author at: Institute of Inorganic Chemistry of the Czech Academy of Sciences, 250 68 Husinec-Řež, Czech Republic.

E-mail address: [henych@iic.cas.cz](mailto:henych@iic.cas.cz) (J. Henych).